This manuscript is the final version of a previous preprint that has undergone peer review, and has been considered for publication to the Seismological Research Letters.

Localized west-dipping seismic structure defines the Elgin–Lugoff Swarm Sequence in South Carolina

Oluwaseyifunmi E. Adeboboye[*1], Lindsay Y. Chuang[1], Miguel Neves[1,2], Zhigang Peng[1], Dan Frost[3], and Steven C. Jaumé[4]

Abstract

An unusual earthquake swarm began in December 2021 between the towns of Elgin and Lugoff in South Carolina, United States. This area is characterized by historically low seismicity, but by April 2024 it has experienced 97 small earthquakes listed in the United States Geological Survey (USGS) catalog, presenting a unique opportunity to investigate the dynamics of earthquake swarms in stable continental regions. These events are located in a north–south diffuse trend, cross-cutting the Eastern Piedmont Fault System, a Late Paleozoic dextral strike-slip fault, however, the location uncertainties were too large to reveal any obvious structure. Starting from October 2022, we deployed 86 Smartsolo 5-Hz 3-component seismic nodes for four months in the direct vicinity of the Elgin swarm. By using a combination of deep learning and match filter techniques for event detection, and double-difference relocation method for precise earthquake locations, we obtain up to 100 high-resolution microearthquake locations, as compared with 4 events listed in the USGS catalog for the deployment period. In our improved catalog, we report significantly smaller magnitudes in comparison to those listed in the USGS catalog, with a local magnitude ranging from -2.17 to 2.54 and achieving a magnitude of completeness at -0.20. The relocated catalog outlined a single fault plane of nearly north–south strike and west–dipping, inconsistent with either known fault strikes or the magnetic anomalies in this region. We also determine focal mechanism solutions for selected events in this swarm sequence, which shows mainly strike-slip faulting with nodal planes aligning with the north–south striking seismic cluster. Our relocated catalog can be used to constrain the location of other swarm events outside the nodal recording period and provide a robust benchmark dataset for further analysis of the swarm sequence.

Introduction

Earthquake swarms are defined as sequences of seismic events closely clustered in both space and time, distinguished by the absence of a single outstanding mainshock (Mogi, 1963). Unlike the mainshock-aftershock sequences which typically follow a power-law decay in the number of seismic events over time (Utsu, 1957), earthquake swarms exhibit an increase in seismic occurrence rate, where the initial event magnitude does not significantly exceed the magnitudes of subsequent large events. They occur worldwide in regions such as volcanic areas, geothermal regions, mid-ocean ridges, and continental rifts (Benoit and McNutt, 1996; Ibs-von Seht et al., 2008; Fischer et al., 2014; Holtkamp and Brudzinski, 2014), and are thought to be primarily driven by external forces such as fluid migrations (Chen et al., 2012; Shelly et al., 2016; Ross et al., 2019, 2020), aseismic slip (Lohman and McGuire, 2007), or dike propagation in volcanic settings (Hill, 1977; Toda et al., 2002), rather than a cascading stress transfer. In complicated models, fluids, aseismic slip or cascade stress triggering may coexist as the driving factors of an earthquake swarm (Fischer and Horálek, 2005; Vidale and Shearer, 2006; Fischer et al., 2014; Danré et al., 2022, 2024).

Intraplate earthquake swarms are distinctive phenomena, and have been observed in several well-known intraplate zones, such as West Bohemia/Vogtland, Canada, Norway, and Greenland (Gregersen, 1979; Atakan et al., 1994; Špičák and Horálek, 2001; Waite and Smith, 2002; Horálek and Fischer, 2008). Additional intraplate earthquake swarm zones influenced by Quaternary volcanism include the French Massif Central, Long Valley in California, the Tengchong volcanic field in Southwestern China, and the Yellowstone volcanic field, which is one of the most seismically active regions in the western U.S (Mazabraud et al., 2005; Vidale and Shearer, 2006; Horálek et al., 2015; Liu et al., 2024; Shelly et al., 2016; Farrell et al., 2009). However, earthquake swarms are rare in the Southeast United States where the background seismicity is generally low. The last time that the southeast U.S. saw an intensive swarm, generating significant public awareness was likely the Norris Lake earthquake swarm about 30 km East of Atlanta, Georgia during the summer of 1993 (Long et al., 1994). Another swarm occurred in Greene County, Alabama in 2014, although the possibility of it being triggered by human activities cannot be completely ruled out (Chen and Wolf, 2018). The causes of intraplate swarms in these regions are often linked to fluid-related processes. One explanation involves the interaction of fluids with regional tectonic stress, which activates pre-existing faults and fractures that are favorably oriented (Špičák, 2000). Another involves fault weakening mechanisms, where chemical and hydrothermal fluid-rock interactions erode fracture walls (Heinicke et al., 2009; Vavryčuk and Hrubcová, 2017).

1. School of Earth and Atmospheric Sciences, Georgia Institute of Technology, USA, https://orcid.org/0009-0007-0302-1084 OEA https://orcid.org/0000-0002-7349-1862 (LYC) https://orcid.org/0000-0002-8581-8551 (MN); 2. Université Côte d'Azur, IRD, CNRS, OCA, Géoazur, Sophia Antipolis, France, https://orcid.org/0000-0002-8581-8551 (MN); 3. School of the Earth, Ocean, and the Environment, College of Arts and Sciences, University of South Carolina, USA, https://orcid.org/0000-0001-7882-5166 (DF); 4. Department of Geology and Environmental Sciences, College of Charleston, USA.
*Corresponding author: oadeboboye3@gatech.edu

At present, our understanding of earthquake swarms is still incomplete, due to our limited capability in detecting/locating microearthquakes and imaging high-resolution fault zone structures, and heterogeneity that play important roles in controlling the fluid pathway and fault slip behaviors (Ross et al., 2020; Liu et al., 2024). Previous studies on swarms are primarily based on standard or relocated earthquake catalogs from seismic network centers (Vidale and Shearer, 2006). However, earthquake catalogs are incomplete and do not include all small earthquakes, especially during large aftershock sequences or intensive earthquake swarms (Kagan, 2004; Peng et al., 2006). Several recent studies on earthquake swarms have utilized either template matching (Peng and Zhao, 2009; Chamberlain et al., 2018; Beaucé et al., 2018), deep-learning techniques (Ross et al., 2018; Zhu et al., 2019; Zhu and Beroza, 2019; Mousavi et al., 2020), or a combination of both (Neves et al., 2024), to detect additional smaller earthquakes that were not listed in standard earthquake catalogs (Shelly et al., 2016; Hotovec-Ellis et al., 2018; Ross et al., 2020). These newly detected/relocated events provide much better constraints on the fault structures and physical processes that drive earthquake swarms.

Starting from December 27, 2021, a prolonged intraplate swarm sequence began with a magnitude 3.3 earthquake between Elgin and Lugoff in South Carolina (Figure 1). In this work, we define this swarm as Elgin or Elgin-Lugoff and use the terms interchangeably throughout the text. South Carolina has experienced similar swarms in the past, such as those related to the impoundment of Lake Monticello in the 1970s, with the largest event being ~M2.9 (Secor Jr et al., 1982). Additional swarm-like events occurred near the lake between 1996 – 1999, and from October to early November 2021 (Chen and Talwani, 2001; Howard et al., 2022). However, what distinguishes the Elgin swarm sequence is its unique location and the occurrence of larger earthquake magnitudes compared to previous swarms in South Carolina (Howard et al., 2022). As of April 2024, 97 microearthquakes were compiled from the United States Geological Survey (USGS) catalog for the Elgin-Lugoff region, with the largest magnitude of 3.6 occurring on June 29, 2022. Similar to other several moderate-sized intraplate earthquakes on the United States East Coast such as the 2011 magnitude 5.8 Virginia earthquake (Chapman, 2013; Meng et al., 2018), the 2014 magnitude 4.1 Edgefield earthquake (Daniels et al., 2019), and the 2020 magnitude 5.2 Sparta earthquake (Figueiredo et al., 2022; Neves et al., 2024), the Elgin-Lugoff swarm occurred in the region surrounding the East Piedmont Fault System (EPFS). This fault system, situated within the United States South Appalachian Piedmont province, is a wide network of ancient faults, characterized by changes in fault styles, inherited structures, and reactivation over time (Howard et al., 2022). Associated with magnetic anomalies that align with the north-east to south-west regional Appalachian trend, the EPFS consists of linear shear zones that have undergone multiple deformation phases, resulting in variable thickness and dip (Hatcher et al., 1977). Specifically, the Elgin-Lugoff swarm is confined within the Modoc Fault Zone of the EPFS, which is a nearly ductile shear zone ranging from 1 to 5 kilometers in thickness (Shah et al., 2023). The shear criteria indicate that it has mainly experienced Alleghanian dextral strike-slip displacement (Hatcher et al., 1977).

Despite being situated within the East Piedmont Fault System, on closer examination, most events in the Elgin-Lugoff swarm sequence appeared to occur in a diffuse zone at a high angle to the known faults rather than along the East Piedmont

Fault System itself (Howard et al., 2022). The intriguing nature of the swarm sequence presents challenges for interpreting the tectonic structures hosting this sequence due to the small magnitudes of the events, the relatively sparse seismic network, and the poorly defined local seismic structure. Additionally, the interpretation may be affected by a potential bias in the cataloged event locations arising from a generic seismic velocity model used in this region. Unlike the Summerville/Charleston region farther south of Elgin, which hosts the Middleton Summerville Seismic Zone and lies within the Outer Coastal Plain, the Elgin swarm resides within the Carolina Sandhills and thus represents significantly different geologic and seismic structures, with a fault system that is not connected to any faults near the Summerville/Charleston region.

Although the Elgin earthquake sequence has not caused significant damage or injuries, it serves as a reminder that earthquakes can occur in unexpected places. Unlike regions such as the Summerville/Charleston area of South Carolina, where historically large earthquakes have occurred in the past, or near Lake Monticello with ongoing swarm-like activities, residents in the Elgin and Lugoff region were unfamiliar with earthquake shaking. This swarm sequence hence provides a rare window of opportunity to study the physical mechanisms of swarms in intraplate regions. It also offers a unique teachable moment to raise earthquake awareness in this region.

In October 2022, 86 SmartSolo nodes (Figure 1) were deployed in Elgin, South Carolina, to record the swarm sequence (Peng et al., 2023). This passive source experiment aims to address several critical questions: What is causing this swarm in an otherwise tectonically quiet region? Is the zone of seismicity as diffuse as it appears, and what is the state of seismic stress in Elgin? In this study, we present the network geometry, and observations of waveforms and other metrics in comparison with nearby broadband recordings. In addition, we apply a combination of machine-learning phase-picking and matched-filter detection to enhance the event detection using up to 4 months of continuous waveform data. We also determine the magnitudes of newly detected events and relocate them with a double difference method to obtain a high-resolution catalog during this period. This experiment seeks to improve the spatial and temporal resolution of the swarm, enabling a deeper understanding of its origins.

Data and Methods

Instrument Deployment and Data Quality

Each node had a 15-day internal battery and was connected to a ~100-day external battery pack, allowing them to record continuously for up to 4 months. Such a long duration was extremely valuable since the seismicity rate of the swarm sequence had already decreased by the time of the deployment. The instrument gain was set to 24 dB, and the sampling rate was 250 Hz. In addition to the 86 nodes, South Carolina Seismic Network (SCSN, network code CO) staff deployed a broadband seismometer JKYD, co-located ~1ft with the seismic node station GT086. They previously deployed the strong motion station BARN following the first event in December 2021, just south of the swarm, which has proven to be valuable for recording the subsequent episodes in May and June 2022. Seismic data from both JKYD and BARN can be accessed in real-time from EarthScope Data Management Center (`https://ds.iris.edu/mda/CO/`). As opposed to the JKYD and BARN stations,

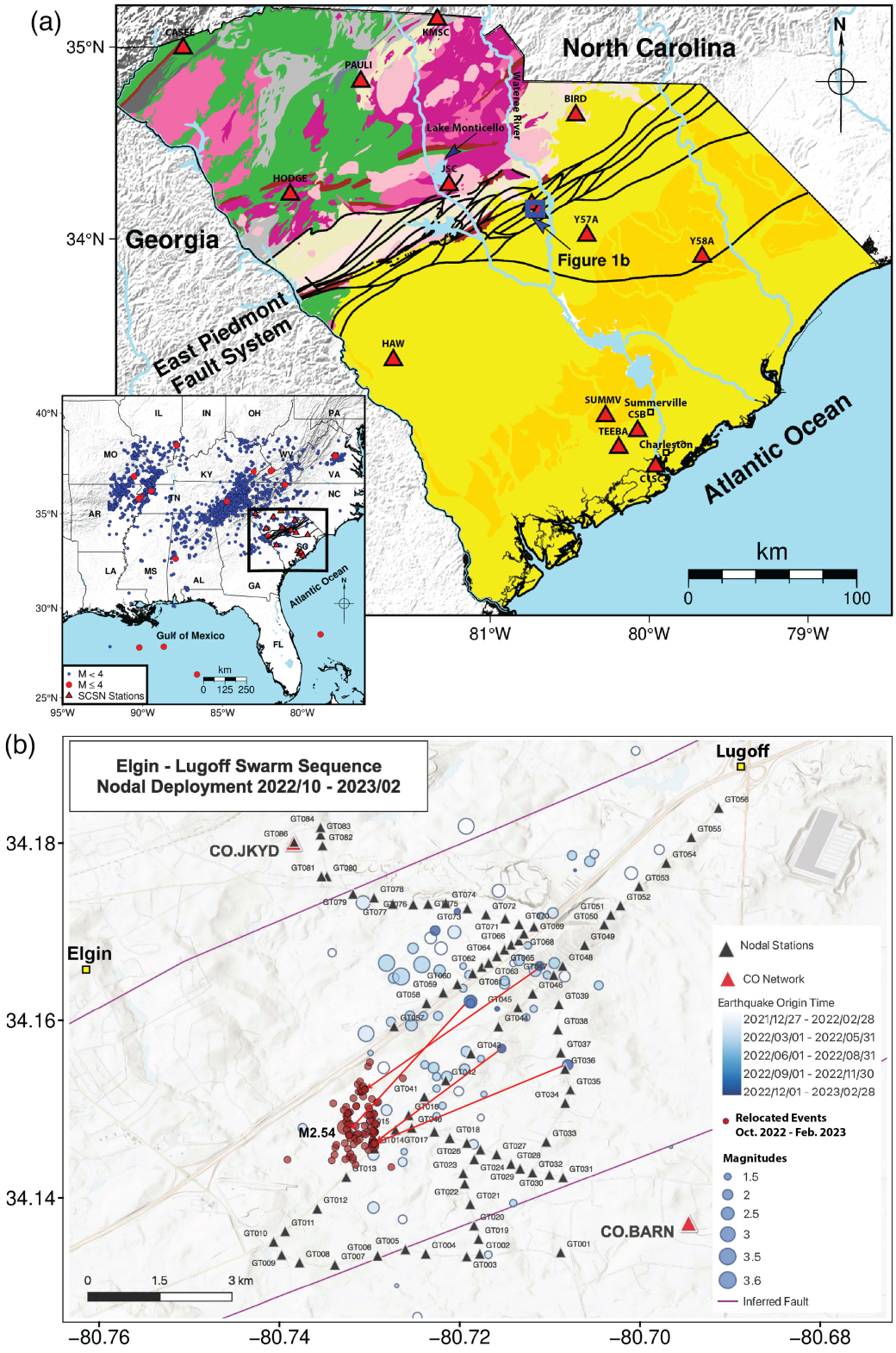

Figure 1: Spatial distribution of the 86 SmartSolo nodes, stations in the South Carolina Seismic Network (SCSN), Central and Eastern US Network (CEUSN, network code N4), and ~ 85 swarm events recorded by the USGS from December 27, 2021 to January 20, 2023. (a) The geologic map of South Carolina (Horton et al., 2017), showing the NE–SW structural features of the East Piedmont Fault System in black. Red triangles correspond to SCSN and CEUSN stations, and the study region is denoted by the blue square (Figure 1b). Inset map displays seismicity in the southeastern United States over the past 20 years. (b) Map of the study region showing the location of the deployed nodal sensors (black triangles) and the event locations. Blue circles represent the events identified in the USGS catalog and the brown circles indicate our ~ 4 months of relocated events, which will be discussed further in the subsequent sections.

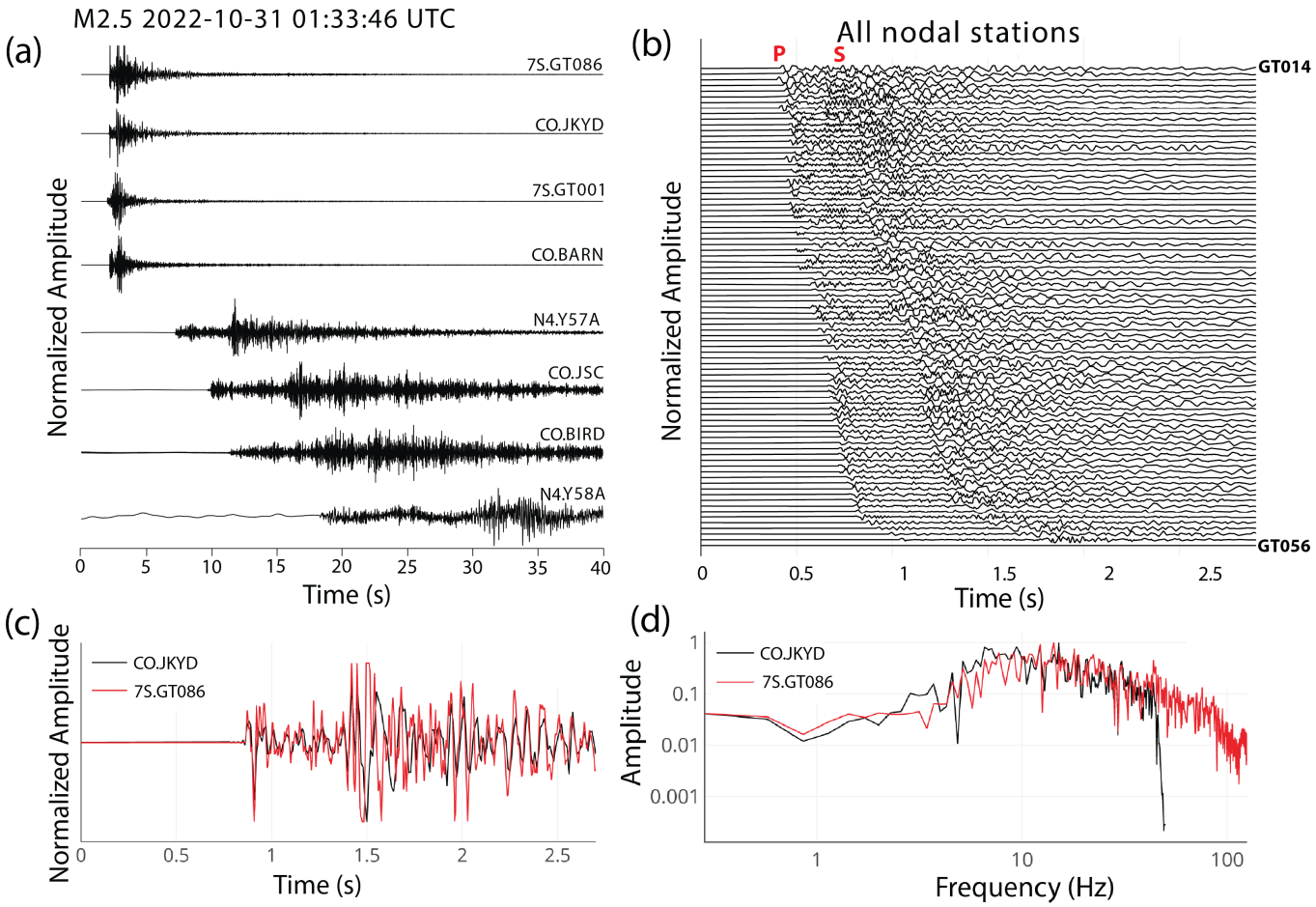

Figure 2: (a) Seismograms comparing recordings between the deployed seismic node stations and regional stations. (b) Normalized vertical component waveforms from all the seismic node stations, plotted by increasing distance from the relocated coordinates. (c) Normalized vertical component waveforms recorded at GT086 and co-located JKYD station after flipping the polarity of the nodal data. (c) Normalized spectra for the vertical components.

the seismic nodes were deployed at shallow, near-surface depths with minimal external protection. One station GT006 was destroyed by a lawnmower shortly after the initial deployment. The remaining 85 nodal seismic stations were retrieved in early February 2023. The total volume of data recovered was about 2 Terabytes.

Figure 2a shows a comparison of waveforms of a magnitude 2.5 event on October 31, 2022 recorded by two nodal seismic stations (GT001 and GT086), two local stations (JKYD and BARN), and by four regional stations. A zoom-in plot of all the seismic node recordings (Figure 2b) shows clear P and S arrivals and possible changes in the relative amplitudes between P and S waves, which can be used to constrain their focal mechanisms. As expected, the waveforms from the co-located GT086 and JKYD station match very well, after we manually flip the polarity of the seismic node recordings (Figure 2c). The reason for such a polarity flip is that for the seismic node recordings, its positive is downward, rather than upwards as in most broadband recordings. As per manufacturer specification, this polarity flip is not present at frequencies below 1-Hz, due to the instrument response of the nodal geophones. In addition, their normalized spectra for this event also match well (Figure 2d), except that the spectrum of the nodal recording goes to 125 Hz, since the nodal data is recorded at 250 sample/s. We

noticed that a portion of the nodal recordings clipped slightly (Figure 2c), likely because the event was relatively shallow, and the gain of the nodal recording was set as 24, the highest value for the nodal sensor recordings. Nonetheless, this demonstrates the similarity between these nodes and the broadband recordings when resolving small earthquakes and shows the quality of this data. We also compared background noise levels using probabilistic power spectral density (PPSD) analysis (Peterson et al., 1993) of signals recorded by our Smart-solo 3C nodal sensors against reference data from JKYD. For our study, the computation of PPSD was carried out for one-month data. The PPSD of background noise recorded at both JKYD and the nearby seismic node station GT086 for all three components (Figure 3, Figure S1), indicate that the frequency response of the noise and amplitude is consistent with the broadband station down to 0.1 Hz. However, at frequencies below 0.1Hz, the seismic nodes exhibit high noise levels. In addition to the inherent sensitivity of the seismic nodes, their shallow deployment depths likely contribute to this increased noise at low frequencies, as they are more exposed to surface disturbances such as wind and human activity. The PPSD results suggest that seismic node stations are not well-suited for accurately recording long-period seismic waves. Nonetheless, given this study's focus on local earthquakes, which are characterized by higher frequencies, these stations prove highly effective for data acquisition and good data quality.

1D Velocity Structure Inversion

To construct the 1D velocity model, we used a combination of historical seismicity in the southeastern US observed at the SCSN and CEUSN stations (Figure 1a), and events from during the swarm recorded at both the SCSN and CEUSN stations, and the nodal array. For the historical seismicity, we used the USGS reported pick times while for the swarm events we manually re-picked the data to identify the P- and S-wave arrival times. Overall, we used 89 events from the swarm.

We inverted for the 1-D velocity structure using VELEST (Kissling et al., 1994). As our initial model, we used that of Charleston, South Carolina, which has 9 velocity layers including a 700 m upper sediment layer. We fixed the Vp/Vs ratio to 1.73 and varied the interface depths manually, while allowing the inversion to fit the velocities. Acknowledging that the historical seismicity generally included earthquakes at greater distances from the stations while the swarm events included earthquakes only at shorter distances, we first inverted for the upper 3 layers of the model using the swarm events alone, then fixed these layers and inverted for the deeper structure using the historical seismicity. The initial and final 1-D velocity model can be found in Tables S1 & S2. As expected, we find that the data are best fit by a velocity model with a thinner sediment layer than the initial Charleston model, with higher basement velocities beneath.

Event Detection & Location

In this part of the study, we followed the steps outlined in (Neves et al., 2024) to perform earthquake detection and relocation. First, we picked P and S arrivals from continuous waveforms of the seismic nodes with the EQtransformer deep learning model (Mousavi et al., 2020), which has been pre-trained on the STanford Earthquake Dataset (Mousavi et al., 2019) within the Seisbench (Woollam et al., 2022) deep learning toolbox. EQtransformer generates three key predictions: the probability

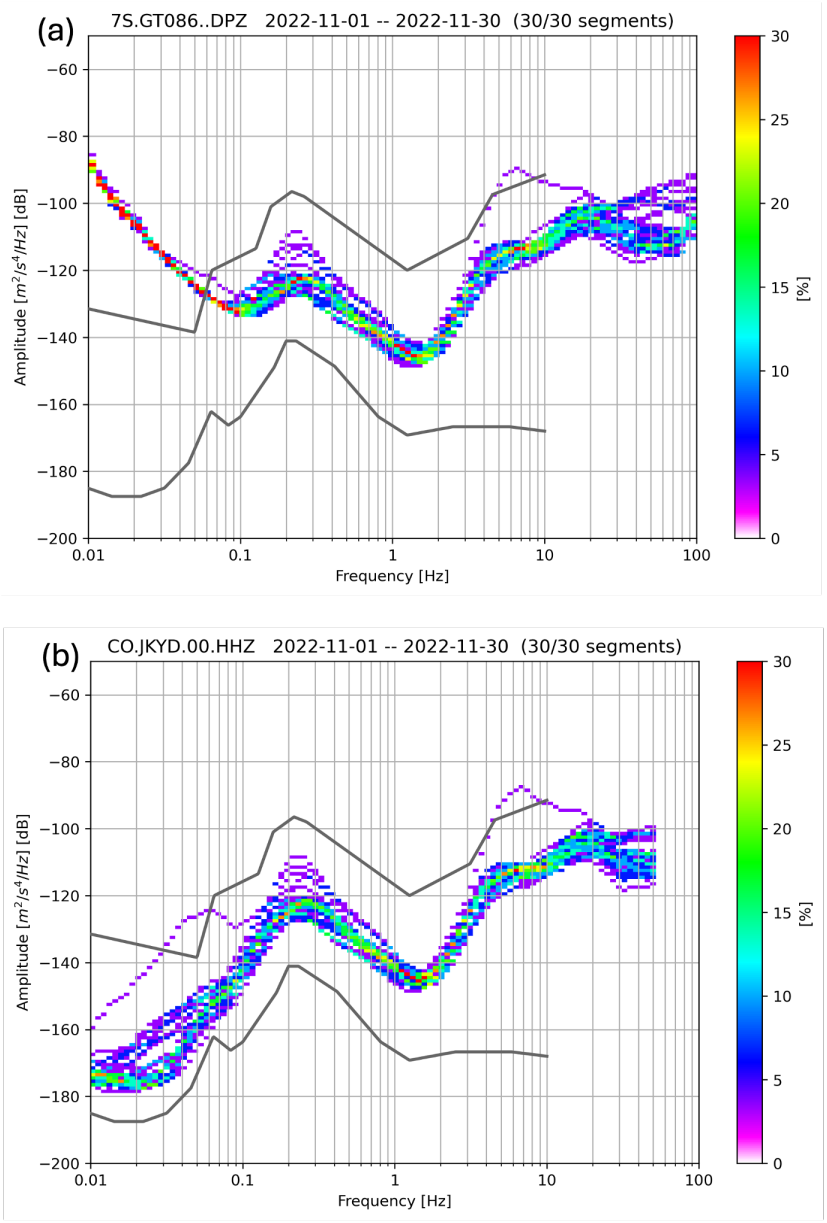

Figure 3: (a) The probabilistic power spectral density (PPSD) of background noise recorded at the (a) broadband seismometer JKYD and (b) GT086. The low and high noise models from (Peterson et al., 1993) are shown as gray curves for reference. The PPSD is computed for the vertical component of the station's recordings.

of event detection and the arrival times of P and S waves within a specific time window. The detected P and S phases (Figure 4a) were grouped as part of an event when the absolute differences in P-wave arrival times between station pairs were 0.7 seconds or less, and the event was detected across at least seven stations. Subsequently, the detected S-waves corresponding to those events were recorded. This criteria helped to eliminate false positives and was easily implemented due to the relatively low number of detections from EQtransformer. Subsequently, phase arrivals that EQTransformer failed to detect at certain stations within the detection window were manually identified and picked.

Thereafter, we utilized the match filter technique, also known as template matching, to detect additional events, employing those identified through the deep learning approach and the existing 4 USGS recorded events as templates. Template

matching (Gibbons and Ringdal, 2006; Shelly et al., 2007; Peng and Zhao, 2009; Yang et al., 2009; Meng et al., 2012; Skoumal et al., 2015; Ross et al., 2019; Neves et al., 2024) involves cross-correlating template waveforms with daily continuous data to identify similar events with high correlation values. After scanning waveforms across all stations and channels, the correlation traces are stacked to calculate the mean cross-correlation (CC) values. Then, detection thresholds are set using the median absolute deviation (MAD), with events selected when the mean CC values exceed a specified multiple of the MAD. This tunable MAD parameter helps distinguish events from background noise, and when multiple events are detected, the one with the highest correlation is prioritized. In this process, both templates and continuous waveforms were bandpass filtered within the 1–60 Hz range and downsampled to 120 samples/s. Following this, template waveforms were windowed at 2.5s around the local events, 0.3s before and 2.2s after the event origin time. We applied the MAD detection threshold of 14 and a mean CC threshold of 0.2 (Figure 4b & c).

To estimate the magnitudes, we first measured the maximum amplitude on the velocity seismogram around the P arrivals for the vertical and horizontal components in the template and detection events. Next, we calculated the median value of the resulting amplitudes obtained for the templates and detection on the vertical and horizontal components. The local magnitudes of detected arrivals were computed as $M_{\text{detection}} = M_{\text{template}} + \log\left(\frac{A_{\text{detection}}}{A_{\text{template}}}\right)$. This follows the assumption that a tenfold increase in amplitude corresponds to a one-unit increase in the magnitude of the detected event relative to the template magnitude (Peng and Zhao, 2009; Shelly et al., 2016; Yao et al., 2021; Chen et al., 2023).

Once all events within our specified nodal deployment timeframe had been detected, event phase information directly from initial absolute location using HYPOINVERSE-2000 (Klein, 2002) was used to derive the catalog differential times for hypoDD (Waldhauser, 2001), setting a limit of 4 maximum neighboring events and a search radius of 5 km. For waveform cross-correlation differential times, we employed EQCorrscan (Chamberlain et al., 2018), designed to detect and analyze repeating or nearly repeating seismic events. Here, we extracted 0.3 seconds around the P & S arrival on both the vertical and horizontal components. This included 0.1 seconds before the arrival and 0.2 seconds after the arrival, with a shift length of 0.05 seconds. Such a short time window was used to ensure that the correlated arrivals were from similar phases, eliminating interference from different seismic phases. We cross-correlated every event pair in a 3 km radius, and each event pair must have at least 3 differential time measurements. The inversion technique used to invert the event locations is the conjugate gradients method, specifically LSQR (Paige and Saunders, 1982).

Focal Mechanism Solution

To obtain the focal mechanism solutions, we manually picked the first motion polarity measurements on the vertical components and flipped these polarities on the processed waveforms due to the aforementioned polarity flip caused by the instrument response. Following this, we computed the S/P amplitude ratio from the displacement seismograms. For each phase, we measured the full amplitude range of the signal around the arrival by measuring the difference between

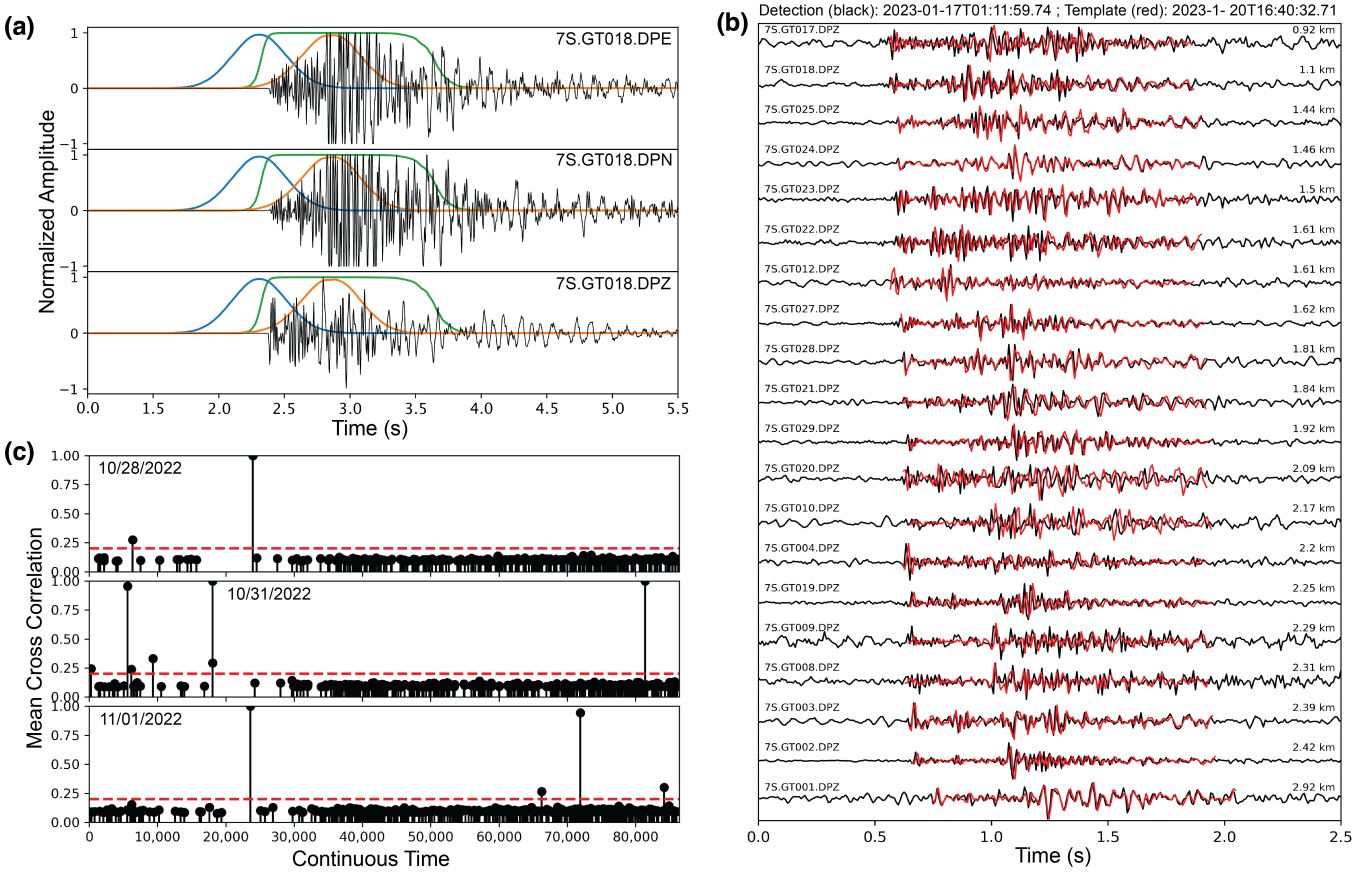

Figure 4: (a) Detection of seismic phase and event using EQTransformer, pre-trained on the STEAD dataset and applied with Seisbench at station GT078 for a M2.5 earthquake occurring on October 31, 2022 (Mousavi et al., 2019, 2020; Woollam et al., 2022). The blue gaussian curve indicates the P-wave arrival, the orange gaussian curve signifies the S-wave arrival, and the green box shape signifies the event detected. Waveforms are ground velocity. (b) Comparison between the ground velocity continuous waveforms (black) and template waveforms (red) within the 1–60Hz range, demonstrating the detection of an event using template matching technique with a mean CC value of 0.77 and MAD value of 79.2. (c) Examples of daily detections from 28 October to 1 November 2022. The dashed line on each plot represents the detection threshold defined by a MAD $\geq$ 14 and mean CC value $\geq$ 0.2.

the maximum and minimum amplitude across all channels, within a time window of -0.01 to 0.5 seconds around the seismic arrival. We then calculated the Euclidean norm of the amplitudes on the different components for each phase $A_{\mathrm{P/S}} = \sqrt{A_N^2 + A_E^2 + A_z^2}$, where N, E and Z are the vertical and horizontal components respectively. Next, the ratio of the S and P amplitude was determined. Similarly, noise amplitudes were calculated using a window from -0.5 to -0.02 seconds before the P-wave arrivals.

Then we determined the take-off angles by integrating our regional crustal velocity model (Table S2) and ak135-f (Kennett et al., 1995) for deeper structures. For focal mechanism inversion, we used the HASH program (Hardebeck and Shearer, 2002, 2003), which takes the polarities, signal displacement amplitude ratios, and take-off angles as input. The criteria set for the HASH algorithm during the moment tensor inversion includes a minimum of 15 polarity observations, a signal-to-noise amplitude ratio not less than 2.0, and a grid search of 15° increments for the strike, dip, and rake to find the set of acceptable focal mechanisms, permitting up to a 20% error in polarity measurements.

Results

Expanding Seismic Catalog through the Detections by the Seismic Nodes

Using only 4 events recorded by the USGS during the seismic nodes deployment timeframe as templates, we detected 26 new local events in the magnitude range of -0.56 to 1.06 using the single station template matching on the broadband JKYD station. Following this, when we used EQTransformer on the continuous waveforms from our seismic nodes, we detected 13 additional events that were not detected using only the JKYD station. For these events with unknown magnitudes, we estimated their magnitudes with a linear regression between the known magnitudes and the logarithm of the mean maximum amplitude of the event after removing the instrument response. Thereafter, we combined the detections of the 39 events as templates to perform match-filter detection across the $\sim$ 4 month nodal deployment recordings.

This expanded the detections of the seismic node stations to a total of 100 microearthquakes (Figure 5a, Table S4). The largest event occurred on October 31, 2022, with a M2.54 and was listed in the USGS catalog. Additionally, the majority of the newly detected events within the swarm display significantly lower magnitudes (M-2.17 to M2.54) than those reported by the USGS during the duration of the nodal deployment, and over the entire observational period of the swarm (Figure 5a).

According to the Gutenberg-Richter (GR) law (Gutenberg, 1944), earthquake magnitudes within a given area follow an exponential distribution, presented by the relation, $\log_{10} N(m) = a - bm$. Here, $N(m)$ represents the count of earthquakes with magnitudes greater or equal to m. Parameters a and b are fixed constants, indicating the overall seismic occurrence rate and the ratio of small to large earthquakes. By using the Maximum Curvature method (Wiemer and Wyss, 2000) with a bin width of 0.1 magnitude units, we estimated the earthquake's magnitude of completeness (M_c) of the nodal deployment as -0.2 and the USGS recorded events over the entire duration of the swarm as 1.90 (Figure 5b), applying a 0.2 correction increase to obtain both values. Given the critical role of selecting an appropriate M_c, which can significantly impact other statistical properties derived from the catalog (Woessner and Wiemer, 2005), we also calculated M_c using the goodness-of-fit method. This involved comparing the observed and synthetic cumulative magnitude frequency distributions at 85% and 90% goodness of fit levels (Wiemer and Wyss, 2000) (Figure 5c). The resulting M_c values were -0.5 for the nodal deployment detected events and 1.7 for the USGS recorded events, similar to the results from the Maximum Curvature method.

Furthermore, using maximum likelihood estimation (Aki, 1965), we determined b-values of 0.66 ± 0.09 and 0.92 ± 0.12 for the nodal and USGS catalogs, based on the M_c values estimated from the Maximum Curvature method. Additionally, we calculated a mean absolute error of 0.09 and 0.25 between the b-values obtained from bootstrapping the magnitude samples and our calculated b-values for the seismic node and USGS catalogs respectively. Our analysis indicates a significant presence of small-magnitude events in the swarm area, suggesting that further investigations are necessary both before and after the nodal deployment to fully understand the dynamics of the swarm sequence. Although b-values of earthquake swarms are often assumed to be greater than 1.0, several studies have observed lower values in intraplate settings such as the Yellowstone earthquake swarms (b-values of 0.6 – 1.5) (Farrell et al., 2009), and intraplate swarms in the West Bohemia/Vogtland region

(b-values of 0.85 – 1.0) (Horálek et al., 2015). Thus, it is not unusual for our swarm observations to show low b-values for both the USGS and nodal deployment catalog. The b-value of the nodal deployment estimates should be considered preliminary due to the simplified estimates of magnitude, and the short time frame of detection (Benz et al., 2015). The lower b-value in our catalog may suggest higher relative stress during our deployment period, as indicated by the larger magnitudes recorded in the USGS catalog following our nodal deployment (Figure 5a). With the detection and observation of a significant increase in the swarm events over an extended period, other reliable methods, such as the b-positive approach (van der Elst, 2021), may be employed to determine the b-value and its temporal evolution.

Seismicity Location and Space-Time Evolution

Using the double-difference technique hypoDD, we obtained and refined the spatial distribution of the 100 swarm events identified during the seismic nodes deployment timeframe. Compared to a broader swarm area reported in the USGS catalog for the entire swarm duration, our analysis revealed a more confined seismogenic zone, prominently showing a single and distinct cluster zone (Figure 1b, Figure 6). The high-resolution of this localized swarm zone is likely a result of the benefit of deploying densely spaced seismic nodes within the Elgin vicinity, unlike the broader network of regional stations that were used to locate events recorded by the USGS throughout the swarm. Specifically, this cluster reflects a nearly north-south trending and steeply west-dipping (72°) seismically active structure (Figure 6c & 7a), with the southern portion spatially aligning and antithetic with one of the magnetic anomalies in the East Piedmont Fault System. The magnetic field data is upward and downward continued to a constant drape of 100 m over topography and reduced-to-pole (Shah et al., 2023).

Predominantly, the relocated swarm activities concentrate at shallow depths between 1.5 to 3.5 km, which is within the depth of the highly folded and faulted Modoc zone. The two seismic streaks observed along the strike direction (Figure 7b) suggest that these are regions on the fault planes where the most prominent stress concentration/asperities reside, at the intersection with the two other faults delineated from the magnetic anomalies. Similar features have been observed in the Heyward Fault Zone and the San Andreas Fault on the west coast of the US (Waldhauser et al., 1999; Rubin et al., 1999; Waldhauser et al., 2004).

Focal mechanism analysis indicates a prevalence of right-lateral strike-slip with minor thrust components, aligning with the Alleghanian strike-slip structures. (Figure 6b & 7a, Table S3). The nodal planes are oriented northeast–southwest and northwest–southeast, with the northeast–southwest striking and east-dipping plane chosen as the preferred nodal plane due to its alignment with the overall orientation of the seismic zone.

Inspired by analyses of other swarms in the Southeastern United States, particularly those in South Carolina and nearby Georgia (Secor Jr et al., 1982; Long et al., 1994), many of which have been associated with fluid activity, we investigated whether fluid migration (Figure 7b), could be influencing the swarm. We explored the possibility of identifying a migration pattern indicative of fluid diffusion (Shapiro et al., 1997). Therefore, we determined the triggering front $r(t) = \sqrt{4\pi Dt}$, where

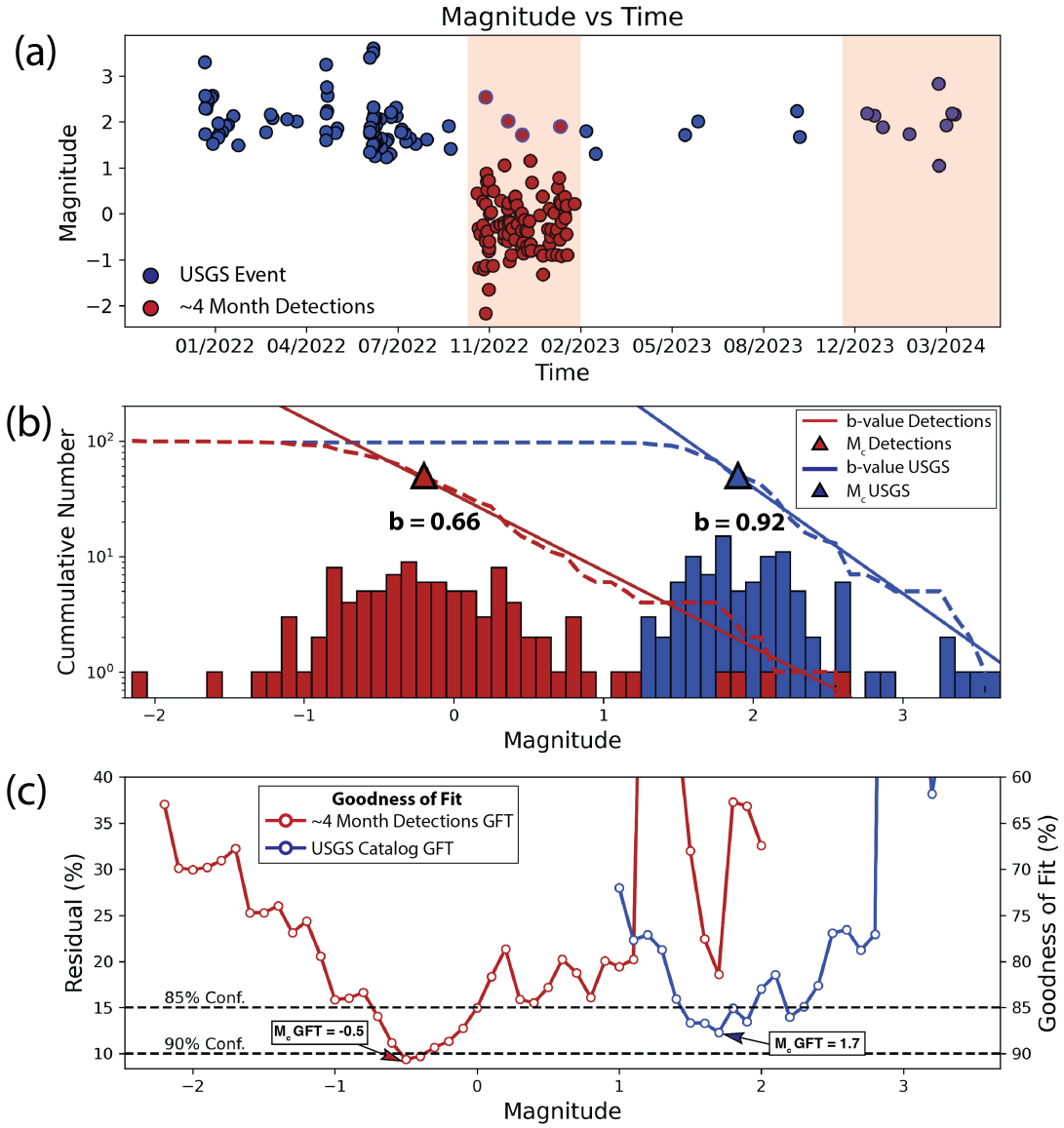

Figure 5: (a) Magnitudes against time for the ~4 month detection with the seismic nodes, and the USGS catalog for the entire duration of the swarm. Brown circles with blue border are events detected by both the nodes and recorded by USGS for the deployment period. (b) GR distribution of the Elgin swarm sequence. The histogram and dashed line represents the discrete and cumulative magnitude frequency distribution. (c) Goodness of fit (GFT) plot estimating the minimum magnitude of completeness. Circles represent the fit between the observed and synthetic cumulative magnitude-frequency distributions. A 95% GFT threshold was not achieved, therefore 90% and 85% were used for the seismic node detections and the USGS catalog, respectively.

t denotes the time since injection began and D is fluid hydraulic diffusivity, assuming that the fluid-saturated medium is uniform and isotropic having a specific point source, which influences the variation in pore pressure (Figure 7c). Ideally, the origin distance and time should be computed relative to the first event that began this swarm sequence, a M3.3 on December 27, 2021, marking the start of the injection point. However, since this event has not been relocated, its timing and location remain uncertain. Therefore, we determined the origin distance and time relative to the first nodal recorded event with a magnitude of 0.45 (M0.45), recorded on October 21, 2022, at 22:21:25.0. Following this, we adopted the methodology

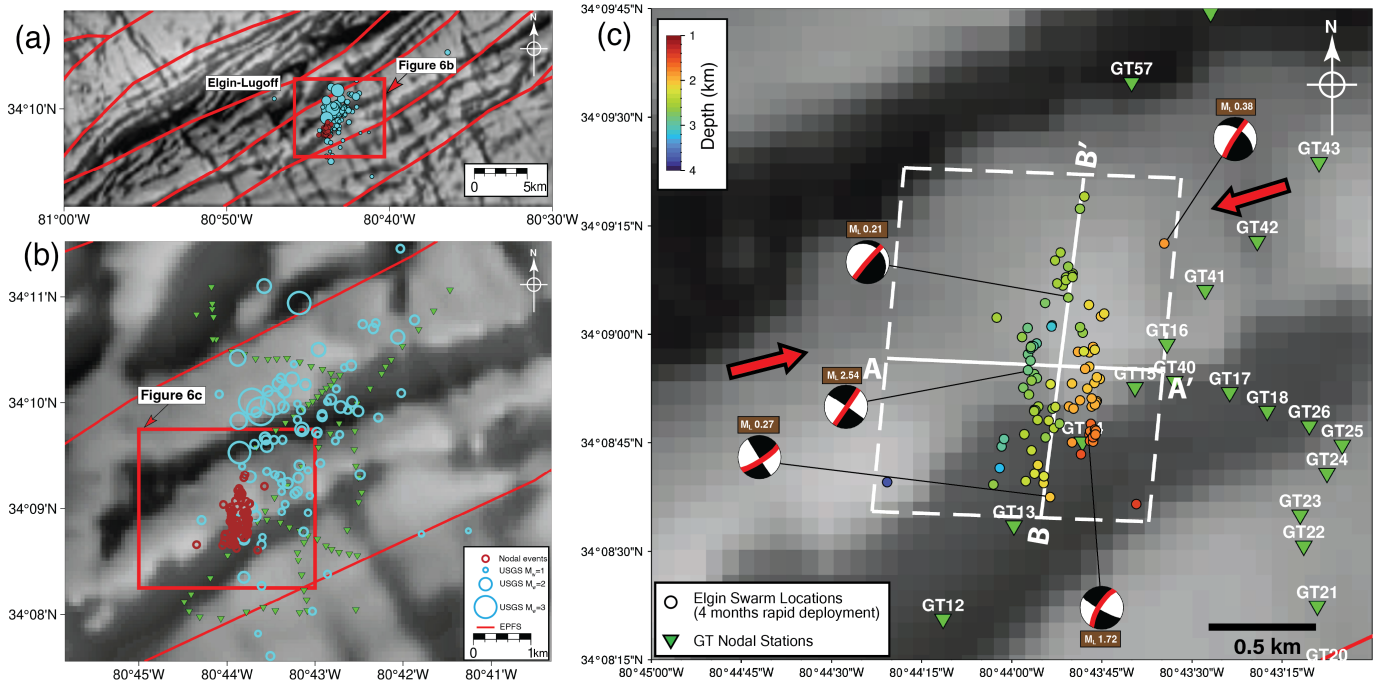

Figure 6: (a) Zoomed-out section of the magnetic lineaments within the EPFS highlighting the general fault trends (red lines) and the placement of swarms within the fault context (Shah et al., 2023). (b) Relocated events identified by the seismic node stations extend beyond a magnetic lineament structure. Cyan circles represent the USGS events while brown circles depict our relocated events. (c) Relocated swarm events are color-coded by depth, with beach balls indicating focal mechanisms and their magnitudes. Preferred nodal planes on focal mechanism solution is highlighted in red. Red arrows depict the maximum principal stress direction (Levandowski et al., 2018), and the white box represents panel in Figure 7a & b.

described in Amezawa et al. (2021). Specifically, we calculated the 90th percentile distance for moving time bins containing five events, with a three-event overlap, to define the triggering fronts. To estimate the hydraulic diffusivity (D), we performed a curve fit, minimizing the sum of squared residuals between the observed and predicted triggering fronts. Since the choice of the end-time for fitting influences the resulting hydraulic diffusivity (Hummel and Shapiro, 2012; Amezawa et al., 2021), we limited the end-time for fitting to 50 days. Using this approach, we estimated a hydraulic diffusivity of 0.014 m^2/s (Figure 7c). However, the data can be better modeled with either a linearly increasing distance versus time or a diminishing distance versus time over this period (Figure 7d). These calculations highlight the challenge of identifying possible driving forces for the Elgin swarm based only on the 4 months of dense-array observation deployed 10 months after the initiation of the swarm.

Discussion & Conclusion

These initial findings present enhanced detection and relocation techniques, increasing seismic event identification from 4 to 100 events over four months. The enhanced catalog for the detections using the seismic nodes predominantly contains smaller magnitude events, with a M_c of -0.20, compared to a M_c of 1.90 of events recorded by the USGS for the entire swarm period (Figure 5b, Table S5). While the Gutenberg-Richter law provides an initial assessment of the frequency-magnitude distribution and parameters such as b-value and M_c, we refrain from heavily relying on it pending a comprehensive detection analysis throughout the entire swarm's duration. The relocated swarm sequence reveals a clear north-south striking and west-

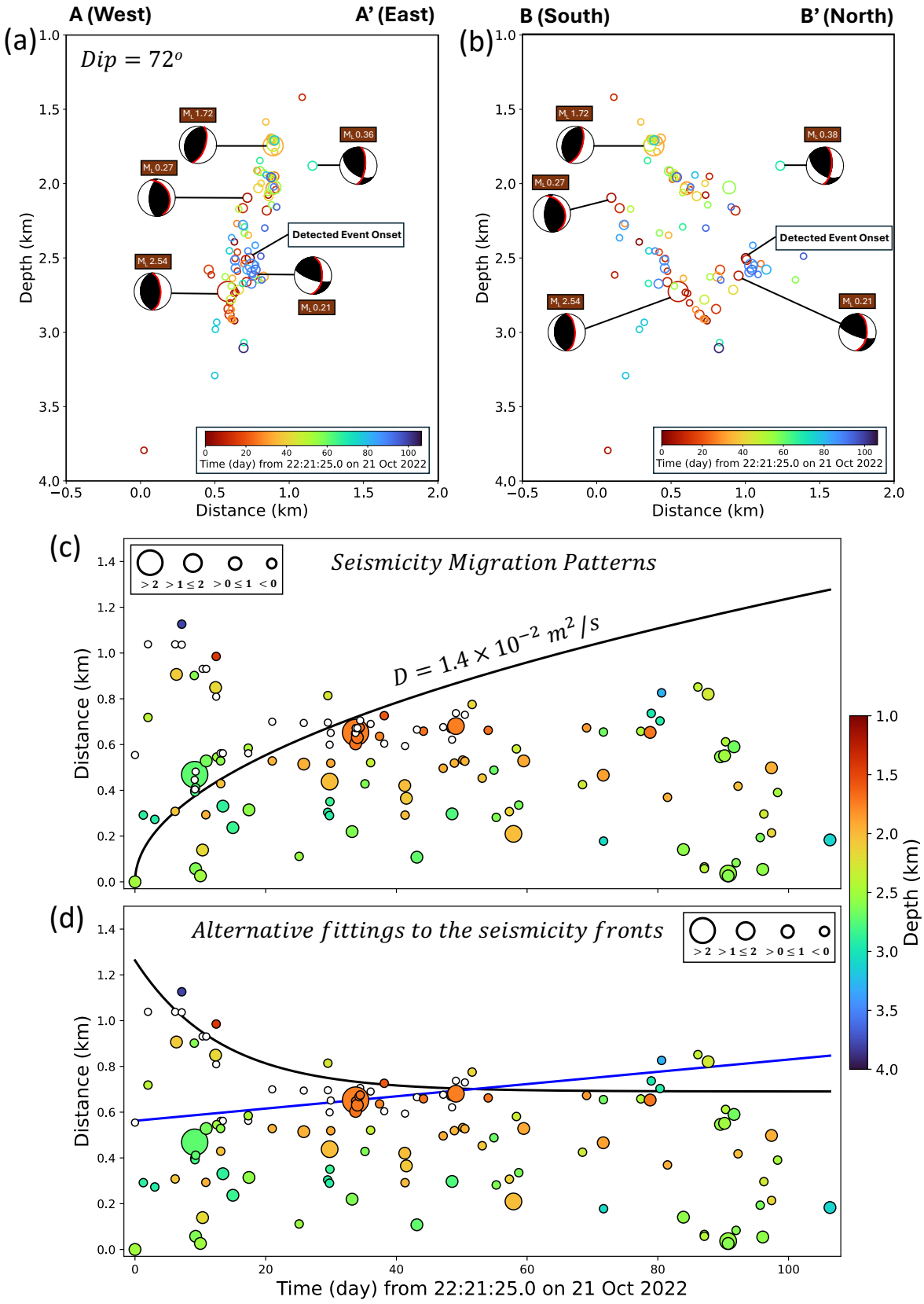

Figure 7: Cross-sectional view of the swarm events and focal mechanisms (Figure 6c), shown in their original orientation as viewed toward geographic north illustrating a structurally west dipping seismic zone. (a) Depth and Temporal Cross-section along the longitudinal axis (A – A') and (b) latitudinal axis (B – B'). (c) Swarm migration over a short-time period modeled with hydraulic diffusivity (D). White circles represent the 90th percentile distance of the triggered fronts during the first 50 days. (d) Two alternative lines to fit the seismicity front.

dipping strike-slip fault structure that hosts the swarm sequence within a confined single cluster, aligning on a conjugate fault relative to the primary EPFS trend (Hatcher et al., 1977) (Figure 6a). This orientation may be favorable for reactivation as this conjugate fault is at an angle to the ENE–WSW oriented principal stress direction in the southeastern United States (Levandowski et al., 2018) (Figure 6c). Although the relocated swarm is shifted to the left and lies outside the current nodal deployment network, we plan to expand the subsequent deployment to cover a broader area, including the region where the relocated events occur. This expansion will incorporate the CO regional stations and use the relocated events to refine the inversion of shallow velocity structures, providing further constraint on the swarm locations.

Although our estimated diffusivity falls within the expected range ($0.01 - 10\ m^2/s$) for swarms observed in other regions (Okada et al., 2012; Shelly et al., 2013; Scholz, 2019; Minetto et al., 2022), and fluid-driven swarms have been identified in nearby areas in South Carolina (Secor Jr et al., 1982; Talwani et al., 2007), we cannot definitely conclude that this swarm is driven by fluid-related processes, as the time-dependent pattern of seismicity during the observed detection timeframe cannot be explained by the diffusion law (Figure 7c). The rather low b-values also make it unclear if it is fluid-driven. It is possible that capturing the entire time of the seismic swarm may explain the migration better, or other possible mechanisms such as aseismic slip or cascade stress triggering could potentially explain the swarm (Vidale and Shearer, 2006; Fischer et al., 2014; Yoshida et al., 2023). However, we only have approximately four months of seismic data, and testing whether aseismic slip is driving the region would require the addition of continuous GPS data, which is not available in this study region as far as we know. In addition, the seismic zone is quite small ~8 km by 6 km according to USGS locations, and even smaller based on our relocations, which could limit the applicability of remote-sensing techniques such as InSAR. We also explored the possibility of cascade triggering, often modeled through Coulomb stress transfer. To investigate this, it would be important to focus on the initial M3.3 event from December 27, 2021, or the largest magnitude event (M3.6) on June 29, 2022. However, due to the potential changes in event locations based on our relocation results, any analysis involving stress triggering should first consider relocating these events to ensure accuracy before further testing. In summary, the physical mechanisms driving this swarm sequence are still not clear.

This study provides a first assessment of the Elgin Swarm and highlights the importance of subsequent efforts focusing on developing a comprehensive catalog for the entire swarm duration combining seismic data from the seismic nodes and regional stations from the SCSN network. Such a catalog will enhance our understanding of the fault's extent and contribute to elucidating the propagation direction and space-time migration, which were not observed during the ~4 months detection since any potential migration patterns are typically detected at the swarm onset (Peng et al., 2024). Subsequent research should consider building on these findings by monitoring hydroseismicity not fully captured by the relocated swarm (Figure 7c) and exploring the influence of water on fault planes (Shelly et al., 2013). Considering the proximity of the Wateree River, fluctuating river discharges and seasonal precipitation may be contributing to the current seismicity (Howard et al., 2022). Research efforts may also expanded to incorporate declustering methods (Zaliapin and Ben-Zion, 2022; Li et al., 2024) to

distinguish between the background seismicity and swarm events before analyzing the potential role of fluid migration or investigating other potential causes of this swarm that have been previously mentioned.

In addition, a resurgence of the swarm sequence has been observed since mid-October 2023 featuring notable seismic events with duration magnitudes of M_d 2.2 and M_d 2.1 on 22 December 2023 at 08:16:43 UTC and 30 December 2023 at 10:27:41 UTC. In response to this activity, we initiated a further deployment from October 2023 involving twenty stations to cover a wider spatial area (Figure S3) and continue monitoring seismic activity within the Elgin-Lugoff region for six months. This expanded data recording and increased area of coverage will contribute to an increase in the number of detections, more precise relocations, and the development of robust and accurate focal mechanisms.

Data and Resources

The 4 months ~2Tb continuous waveforms used for this study will be accessible through the EarthScope Consortium PH5 Web Services (https://service.iris.edu) under the 7S (2022–2023) network (Peng and Frost, 2022). Information of stations for the SCSN and CEUSN used for this research can be accessed with network codes CO and N4, respectively, in the Earthscope Metadata Aggregator (https://doi.org/10.7914/SN/CO, https://doi.org/10.7914/SN/N4). Focal mechanism solutions, MFT detected and relocated catalog can be found in Table S3–S5.

Declaration of Competing Interests

The authors acknowledge that there are no conflicts of interest recorded.

Acknowledgments

We appreciate Dr. Scott Howard's assistance with the deployment of the seismic node stations and his contribution that improved the manuscript. We also thank Dr. Anjana Shah for providing the regional magnetic field anomaly map and express our gratitude to the students from Georgia Institute of Technology, School of Earth and Atmospheric Sciences and the University of South Carolina, School of Earth, Ocean, and Environment for their significant support during the deployment. We extend our sincere gratitude to Dr. Oliver Boyd, Editor for the Eastern Section of SRL, and to the two anonymous reviewers, whose feedback significantly enhanced the quality of this manuscript. Additionally, we thank the Society of Exploration Geophysics' student chapter outreach grant for providing additional financial support to our fieldwork. This work was funded by the National Science Foundation EAR-Geophysics grants (EAR-2322461 and EAR-2321094 to OEA, LYC, MN and ZP, and EAR-2303140 and EAR-2321095 to DF).

References

Aki, K. (1965). Maximum likelihood estimate of b in the formula log n= a-bm and its confidence limits. *Bull. Earthquake Res. Inst., Tokyo Univ.* **43**, 237–239.

Amezawa, Y., T. Maeda, and M. Kosuga (2021). Migration diffusivity as a controlling factor in the duration of earthquake swarms. *Earth, Planets and Space* **73**, 1–11.

Atakan, K., C. D. Lindholm, and J. Havskov (1994). Earthquake swarm in steigen, northern norway: an unusual example of intraplate seismicity. *Terra Nova* **6**(2), 180–194.

Beaucé, E., W. B. Frank, and A. Romanenko (2018). Fast matched filter (fmf): An efficient seismic matched-filter search for both cpu and gpu architectures. *Seismological Research Letters* **89**(1), 165–172.

Benoit, J. P. and S. R. McNutt (1996). Global volcanic earthquake swarm database and preliminary analysis of volcanic earthquake swarm duration. *Annals of Geophysics* **39**(2).

Benz, H. M., N. D. McMahon, R. C. Aster, D. E. McNamara, and D. B. Harris (2015). Hundreds of earthquakes per day: The 2014 guthrie, oklahoma, earthquake sequence. *Seismological Research Letters* **86**(5), 1318–1325.

Chamberlain, C. J., C. J. Hopp, C. M. Boese, E. Warren-Smith, D. Chambers, S. X. Chu, K. Michailos, and J. Townend (2018). Eqcorrscan: Repeating and near-repeating earthquake detection and analysis in python. *Seismological Research Letters* **89**(1), 173–181.

Chapman, M. (2013). On the rupture process of the 23 august 2011 virginia earthquake. *Bulletin of the Seismological Society of America* **103**(2A), 613–628.

Chen, J. and L. W. Wolf (2018). A notable earthquake swarm in alabama: Natural or anthropogenic? *Seismological Research Letters* **89**(4), 1583–1594.

Chen, L. and P. Talwani (2001). Renewed seismicity near monticello reservoir, south carolina, 1996–1999. *Bulletin of the Seismological Society of America* **91**(1), 94–101.

Chen, W., M. Neves, Q. Zhai, C. Daniels, O. Adeboboye, S. Jaume, and Z. Peng (2023). Preliminary results from a dense short-period seismic deployment around the source zone of the 1886 m 7 south carolina earthquake. *Seismological Research Letters* **94**(5), 2479–2488.

Chen, X., P. Shearer, and R. Abercrombie (2012). Spatial migration of earthquakes within seismic clusters in southern california: Evidence for fluid diffusion. *Journal of Geophysical Research: Solid Earth* **117**(B4).

Daniels, C., Z. Peng, Q. Wu, S. Ni, X. Meng, D. Yao, L. S. Wagner, and K. M. Fischer (2019, 11). The 15 February 2014 Mw 4.1 South Carolina Earthquake Sequence: Aftershock Productivity, Hypocentral Depths, and Stress Drops. *Seismological Research Letters* **91**(1), 452–464.

Danré, P., L. De Barros, F. Cappa, and J.-P. Ampuero (2022). Prevalence of aseismic slip linking fluid injection to natural and anthropogenic seismic swarms. *Journal of Geophysical Research: Solid Earth* **127**(12), e2022JB025571.

Danré, P., L. De Barros, F. Cappa, and L. Passarelli (2024). Parallel dynamics of slow slips and fluid-induced seismic swarms. *Nature Communications* **15**(1), 8943.

Farrell, J., S. Husen, and R. B. Smith (2009). Earthquake swarm and b-value characterization of the yellowstone volcano-tectonic system. *Journal of Volcanology and Geothermal Research* **188**(1-3), 260–276.

Figueiredo, P., J. Hill, A. Merschat, C. Scheip, K. Stewart, L. Owen, R. Wooten, M. Carter, E. Szymanski, S. Horton, et al. (2022). The mw 5.1, 9 august 2020, sparta earthquake, north carolina: The first documented seismic surface rupture in the eastern united states. *GSA Today* **32**(3-4).

Fischer, T. and J. Horálek (2005). Slip-generated patterns of swarm microearthquakes from west bohemia/vogtland (central europe): Evidence of their triggering mechanism? *Journal of Geophysical Research: Solid Earth* **110**(B5).

Fischer, T., J. Horálek, P. Hrubcová, V. Vavryčuk, K. Bräuer, and H. Kämpf (2014). Intra-continental earthquake swarms in west-bohemia and vogtland: a review. *Tectonophysics* **611**, 1–27.

Gibbons, S. J. and F. Ringdal (2006). The detection of low magnitude seismic events using array-based waveform correlation. *Geophysical Journal International* **165**(1), 149–166.

Gregersen, S. (1979). Intraplate earthquake swarms in greenland and adjacent continental regions. *Nature* **281**(5733), 661–662.

Gutenberg, B., C. F. R. (1944). Frequency of earthquakes in california. *Bull. Seismol. Soc. Am. 34*, 185–188.

Hardebeck, J. L. and P. M. Shearer (2002). A new method for determining first-motion focal mechanisms. *Bull. Seismol. Soc. Am.* (no. 6), 2264–2276.

Hardebeck, J. L. and P. M. Shearer (2003). Using s/p amplitude ratios to constrain the focal mechanisms of small earthquakes. *Bulletin of the Seismological Society of America* **93**(6), 2434–2444.

Hatcher, Robert D., J., D. E. Howell, and P. Talwani (1977, oct). Eastern piedmont fault system: Speculations on its extent. *Geology* **5**(10), 636.

Heinicke, J., T. Fischer, R. Gaupp, J. Götze, U. Koch, H. Konietzky, and K.-P. Stanek (2009). Hydrothermal alteration as a trigger mechanism for earthquake swarms: the vogtland/nw bohemia region as a case study. *Geophysical Journal International* **178**(1), 1–13.

Hill, D. P. (1977). A model for earthquake swarms. *Journal of Geophysical Research* **82**(8), 1347–1352.

Holtkamp, S. and M. R. Brudzinski (2014). Megathrust earthquake swarms indicate frictional changes which delimit large earthquake ruptures. *Earth and Planetary Science Letters* **390**, 234–243.

Horálek, J. and T. Fischer (2008). Role of crustal fluids in triggering the west bohemia/vogtland earthquake swarms: just what we know (a review). *Studia Geophysica et Geodaetica* **52**(4), 455–478.

Horálek, J., T. Fischer, P. Einarsson, S. Jakobsdótir, M. Beer, I. Kougioumtzoglou, E. Patelli, and S. Au (2015). Earthquake swarms. *Encyclopedia of Earthquake Engineering*, 871–885.

Horton, J. D., C. A. San Juan, and D. B. Stoeser (2017). The state geologic map compilation (sgmc) geodatabase of the conterminous united states. Technical report, US Geological Survey.

Hotovec-Ellis, A. J., D. R. Shelly, D. P. Hill, A. M. Pitt, P. B. Dawson, and B. A. Chouet (2018). Deep fluid pathways beneath mammoth mountain, california, illuminated by migrating earthquake swarms. *Science Advances* **4**(8), eaat5258.

Howard, C. S., S. Jaume, S. M. White, and P. Talwani (2022). Report on elgin-area earthquakes. Technical report, South Carolina Department of Natural Resources.

Hummel, N. and S. Shapiro (2012). Microseismic estimates of hydraulic diffusivity in case of non-linear fluid-rock interaction. *Geophysical Journal International* **188**(3), 1441–1453.

Ibs-von Seht, M., T. Plenefisch, and K. Klinge (2008). Earthquake swarms in continental rifts—a comparison of selected cases in america, africa and europe. *Tectonophysics* **452**(1-4), 66–77.

Kagan, Y. Y. (2004). Short-term properties of earthquake catalogs and models of earthquake source. *Bulletin of the Seismological Society of America* **94**(4), 1207–1228.

Kennett, B. L., E. R. Engdahl, and B. R. (1995). Constraints on seismic velocities in the earth from travel times. *Geophys. J. Int.*, 108–124.

Kissling, E., W. Ellsworth, D. Eberhart-Phillips, and U. Kradolfer (1994). Initial reference models in local earthquake tomography. *Journal of Geophysical Research: Solid Earth* **99**(B10), 19635–19646.

Klein, F. W. (2002). User's guide to hypoinverse-2000, a fortran program to solve for earthquake locations and magnitudes. Technical report, US Geological Survey.

406 Levandowski, W., R. B. Herrmann, R. Briggs, O. Boyd, and R. Gold (2018). An updated stress map of the continental united states reveals
407 heterogeneous intraplate stress. *Nature Geoscience* **11**(6), 433–437.
408 Li, L., B. Wang, Z. Peng, J. Hou, and F. Wang (2024). Statistical features of seismicity associated with large earthquakes on the chinese
409 continent between 2008 and 2019 based on newly detected catalogs. *Seismological Research Letters* **95**(3), 1701–1717.
410 Liu, M., Y. J. Tan, X. Lei, H. Li, Y. Zhang, and W. Wang (2024). Intersection between tectonic faults and magmatic systems promotes
411 swarms with large-magnitude earthquakes around the tengchong volcanic field, southeastern tibetan plateau. *Geology* **52**(4), 302–307.
412 Lohman, R. B. and J. J. McGuire (2007). Earthquake swarms driven by aseismic creep in the salton trough, california. *Journal of Geophysical*
413 *Research: Solid Earth* **112**(B4).
414 Long, L., A. Kocaoglu, R. Hawman, and P. Gore (1994). The norris lake earthquake swarm of june through september, 1993; preliminary
415 findings. *Seismological Research Letters* **65**(2), 167–171.
416 Mazabraud, Y., N. Béthoux, and S. Deroussi (2005). Characterisation of the seismological pattern in a slowly deforming intraplate region:
417 Central and western france. *Tectonophysics* **409**(1-4), 175–192.
418 Meng, X., H. Yang, and Z. Peng (2018). Foreshocks, b value map, and aftershock triggering for the 2011 mw 5.7 virginia earthquake. *Journal*
419 *of Geophysical Research: Solid Earth* **123**(6), 5082–5098.
420 Meng, X., X. Yu, Z. Peng, and B. Hong (2012, 12). Detecting earthquakes around salton sea following the 2010 mw7.2 el mayor-cucapah
421 earthquake using gpu parallel computing. *Procedia Computer Science* **9**, 937–946.
422 Minetto, R., A. Helmstetter, S. Schwartz, M. Langlais, J. Nomade, and P. Guéguen (2022). Analysis of the spatiotemporal evolution of the
423 maurienne swarm (french alps) based on earthquake clustering. *Earth and Space Science* **9**(7), e2021EA002097.
424 Mogi, K. (1963). Some discussions on aftershocks, foreshocks and earthquake swarms-the fracture of a semi finite body caused by an inner
425 stress origin and its relation to the earthquake phenomena. *Bull. Earthq. Res. Inst.* **41**, 615–658.
426 Mousavi, S. M., W. L. Ellsworth, W. Zhu, L. Y. Chuang, and G. C. Beroza (2020, 08). Earthquake transformer—an attentive deep-learning
427 model for simultaneous earthquake detection and phase picking. *Nature Communications* **11**(1), 3952.
428 Mousavi, S. M., Y. Sheng, W. Zhu, and G. C. Beroza (2019). Stanford earthquake dataset (stead): A global data set of seismic signals for ai.
429 *IEEE Access*.
430 Neves, M., L. Y. Chuang, W. Li, Z. Peng, P. M. Figueiredo, and S. Ni (2024). Complex rupture dynamics of the extremely shallow august
431 2020 m5. 1 sparta, north carolina earthquake. *Communications Earth & Environment* **5**(1), 163.
432 Okada, T., T. Matsuzawa, N. Umino, K. Yoshida, A. Hasegawa, H. Takahashi, T. Yamada, M. Kosuga, T. Takeda, A. Kato, et al. (2012).
433 Hypocenter migration and crustal seismic velocity distribution observed for the inland earthquake swarms induced by the 2011 tohoku-
434 oki earthquake in ne japan: Implications for crustal fluid distribution and crustal permeability. *Crustal Permeability*, 307–323.
435 Paige, C. C. and M. A. Saunders (1982, mar). Lsqr: An algorithm for sparse linear equations and sparse least squares. *ACM Trans. Math.*
436 *Softw.* **8**(1), 43–71.
437 Peng, Z., L. Chuang, P. Mach, D. Frost, S. Howard, and S. White (2023, April). High-resolution imaging of the elgin-lugoff earthquake swarm
438 sequence in south carolina using a dense seismic nodal array. In *Annual Meeting of the Seismological Society of America*. Seismological
439 Society of America: Springer.
440 Peng, Z. and D. Frost (2022). Nodal deployment for the elgin-lugoff south carolina earthquake swarm.

Peng, Z., X. Lei, Q.-Y. Wang, D. Wang, P. Mach, D. Yao, A. Kato, K. Obara, and M. Campillo (2024). The evolution process between the earthquake swarm beneath the noto peninsula, central japan and the 2024 m 7.6 noto hanto earthquake sequence. *Earthquake Research Advances*, 100332.

Peng, Z., J. E. Vidale, and H. Houston (2006). Anomalous early aftershock decay rate of the 2004 mw6. 0 parkfield, california, earthquake. *Geophysical Research Letters* **33**(17).

Peng, Z. and P. Zhao (2009). Migration of early aftershocks following the 2004 parkfield earthquake. *Nature Geoscience* **2**(12), 877–881.

Peterson, J. et al. (1993). *Observations and modeling of seismic background noise*, Volume 93. US Geological Survey Reston, VA, USA.

Ross, Z. E., E. S. Cochran, D. T. Trugman, and J. D. Smith (2020). 3d fault architecture controls the dynamism of earthquake swarms. *Science* **368**(6497), 1357–1361.

Ross, Z. E., M.-A. Meier, and E. Hauksson (2018). P wave arrival picking and first-motion polarity determination with deep learning. *Journal of Geophysical Research: Solid Earth* **123**(6), 5120–5129.

Ross, Z. E., D. T. Trugman, E. Hauksson, and P. M. Shearer (2019). Searching for hidden earthquakes in southern california. *Science* **364**(6442), 767–771.

Rubin, A. M., D. Gillard, and J.-L. Got (1999). Streaks of microearthquakes along creeping faults. *Nature* **400**(6745), 635–641.

Scholz, C. H. (2019). *The mechanics of earthquakes and faulting*. Cambridge university press.

Secor Jr, D. T., L. S. Peck, D. M. Pitcher, D. C. Prowell, D. H. Simpson, W. A. Smith, and A. W. Snoke (1982). Geology of the area of induced seismic activity at monticello reservoir, south carolina. *Journal of Geophysical Research: Solid Earth* **87**(B8), 6945–6957.

Shah, A. K., T. L. Pratt, and J. W. Horton Jr (2023). Rift basins and intraplate earthquakes: New high-resolution aeromagnetic data provide insights into buried structures of the charleston, south carolina seismic zone. *Geochemistry, Geophysics, Geosystems* **24**(5), e2022GC010803.

Shapiro, S. A., E. Huenges, and G. Borm (1997). Estimating the crust permeability from fluid-injection-induced seismic emission at the ktb site. *Geophysical Journal International* **131**(2), F15–F18.

Shelly, D. R., G. C. Beroza, and S. Ide (2007). Non-volcanic tremor and low-frequency earthquake swarms. *Nature* **446**(7133), 305–307.

Shelly, D. R., W. L. Ellsworth, and D. P. Hill (2016). Fluid-faulting evolution in high definition: Connecting fault structure and frequency-magnitude variations during the 2014 long valley caldera, california, earthquake swarm. *Journal of Geophysical Research: Solid Earth* **121**(3), 1776–1795.

Shelly, D. R., D. P. Hill, F. Massin, J. Farrell, R. B. Smith, and T. Taira (2013). A fluid-driven earthquake swarm on the margin of the yellowstone caldera. *J. Geophys. Res. Solid Earth* **118**, 4872–4886.

Skoumal, R. J., M. Brudzinski, and B. Currie (2015). Distinguishing induced seismicity from natural seismicity in ohio: Demonstrating the utility of waveform template matching. *Journal of geophysical Research Solid Earth* **120**, 6284–6296.

Špičák, A. (2000). Earthquake swarms and accompanying phenomena in intraplate regions: a review. *Studia Geophysica et Geodaetica* **44**, 89–106.

Špičák, A. and J. Horálek (2001). Possible role of fluids in the process of earthquake swarm generation in the west bohemia/vogtland seismoactive region. *Tectonophysics* **336**(1-4), 151–161.

Talwani, P., L. Chen, and K. Gahalaut (2007). Seismogenic permeability, ks. *Journal of Geophysical Research: Solid Earth* **112**(B7).

Toda, S., R. S. Stein, and T. Sagiya (2002). Evidence from the ad 2000 Izu islands earthquake swarm that stressing rate governs seismicity. *Nature* **419**(6902), 58–61.

Utsu, T. (1957). Magnitudes of earthquakes and occurrence of their aftershocks. *Zisin* **10**(1), 35–45.

van der Elst, N. J. (2021). B-positive: A robust estimator of aftershock magnitude distribution in transiently incomplete catalogs. *Journal of Geophysical Research: Solid Earth* **126**(2), e2020JB021027.

Vavryčuk, V. and P. Hrubcová (2017). Seismological evidence of fault weakening due to erosion by fluids from observations of intraplate earthquake swarms. *Journal of Geophysical Research: Solid Earth* **122**(5), 3701–3718.

Vidale, J. E. and P. M. Shearer (2006). A survey of 71 earthquake bursts across southern california: Exploring the role of pore fluid pressure fluctuations and aseismic slip as drivers. *Journal of Geophysical Research: Solid Earth* **111**(B5).

Waite, G. P. and R. B. Smith (2002). Seismic evidence for fluid migration accompanying subsidence of the yellowstone caldera. *Journal of Geophysical Research: Solid Earth* **107**(B9), ESE–1.

Waldhauser, F. (2001). hypodd-a program to compute double-difference hypocenter locations. *USGS Publications Warehouse*.

Waldhauser, F., W. Ellsworth, D. P. Schaff, and A. Cole (2004). Streaks, multiplets, and holes: High-resolution spatio-temporal behavior of parkfield seismicity. *Geophysical Research Letters* **31**(18).

Waldhauser, F., W. L. Ellsworth, and A. Cole (1999). Slip-parallel seismic lineations on the northern hayward fault, california. *Geophysical research letters* **26**(23), 3525–3528.

Wiemer, S. and M. Wyss (2000). Minimum magnitude of completeness in earthquake catalogs: Examples from alaska, the western united states, and japan. *Bulletin of the Seismological Society of America* **90**(4), 859–869.

Woessner, J. and S. Wiemer (2005). Assessing the quality of earthquake catalogues: Estimating the magnitude of completeness and its uncertainty. *Bulletin of the Seismological Society of America* **95**(2), 684–698.

Woollam, J., J. Münchmeyer, F. Tilmann, A. Rietbrock, and D. Lange (2022, 03). Seisbench — a toolbox for machine learning in seismology. *Seismologial Research Letters* **93**, 1695–1709.

Yang, H., L. Zhu, and R. Chu (2009). Fault-plane determination of the 18 april 2008 mount carmel, illinois, earthquake by detecting and relocating aftershocks. *Bulletin of the Seismological Society of America* **99**(6), 3413–3420.

Yao, D., Y. Huang, and J. L. Fox (2021). New insights into the lake erie fault system from the 2019 ml 4.0 ohio earthquake sequence. *Seismological Society of America* **92**(4), 2531–2539.

Yoshida, K., M. Uno, T. Matsuzawa, Y. Yukutake, Y. Mukuhira, H. Sato, and T. Yoshida (2023). Upward earthquake swarm migration in the northeastern noto peninsula, japan, initiated from a deep ring-shaped cluster: Possibility of fluid leakage from a hidden magma system. *Journal of Geophysical Research: Solid Earth* **128**(6), e2022JB026047.

Zaliapin, I. and Y. Ben-Zion (2022). Perspectives on clustering and declustering of earthquakes. *Seismological Research Letters* **93**(1), 386–401.

Zhu, L., Z. Peng, J. McClellan, C. Li, D. Yao, Z. Li, and L. Fang (2019). Deep learning for seismic phase detection and picking in the aftershock zone of 2008 mw7. 9 wenchuan earthquake. *Physics of the Earth and Planetary Interiors* **293**, 106261.

Zhu, W. and G. C. Beroza (2019). Phasenet: a deep-neural-network-based seismic arrival-time picking method. *Geophysical Journal International* **216**(1), 261–273.

Figure Legends

Figure 1: Spatial distribution of the 86 SmartSolo nodes, stations in the South Carolina Seismic Network (SCSN), Central and Eastern US Network (CEUSN, network code N4), and ~ 85 swarm events recorded by the USGS from December 27, 2021 to January 20, 2023. (a) The geologic map of South Carolina (Horton et al., 2017), showing the NE–SW structural features of the East Piedmont Fault System in black. Red triangles correspond to SCSN and CEUSN stations, and the study region is denoted by the blue square (Figure 1b). Inset map displays seismicity in the southeastern United States over the past 20 years. (b) Map of the study region showing the location of the deployed nodal sensors (black triangles) and the event locations. Blue circles represent the events identified in the USGS catalog and the brown circles indicate our ~ 4 months of relocated events, which will be discussed further in the subsequent sections.

Figure 2: (a) Seismograms comparing recordings between the deployed seismic node stations and regional stations. (b) Normalized vertical component waveforms from all the seismic node stations, plotted by increasing distance from the relocated coordinates. (c) Normalized vertical component waveforms recorded at GT086 and co-located JKYD station after flipping the polarity of the nodal data. (c) Normalized spectra for the vertical components.

Figure 3: (a) The probabilistic power spectral density (PPSD) of background noise recorded at the (a) broadband seismometer JKYD and (b) GT086. The low and high noise models from (Peterson et al., 1993) are shown as gray curves for reference. The PPSD is computed for the vertical component of the station's recordings.

Figure 4: (a) Detection of seismic phase and event using EQTransformer, pre-trained on the STEAD dataset and applied with Seisbench at station GT078 for a M2.5 earthquake occurring on October 31, 2022 (Mousavi et al., 2019, 2020; Woollam et al., 2022). The blue gaussian curve indicates the P-wave arrival, the orange gaussian curve signifies the S-wave arrival, and the green box shape signifies the event detected. Waveforms are ground velocity. (b) Comparison between the ground velocity continuous waveforms (black) and template waveforms (red) within the 1–60Hz range, demonstrating the detection of an event using template matching technique with a mean CC value of 0.77 and MAD value of 79.2. (c) Examples of daily detections from 28 October to 1 November 2022. The dashed line on each plot represents the detection threshold defined by a MAD $\geq$ 14 and mean CC value $\geq$ 0.2.

Figure 5: (a) Magnitudes against time for the ~4 month detection with the seismic nodes, and the USGS catalog for the entire duration of the swarm. Brown circles with blue border are events detected by both the nodes and recorded by USGS for the deployment period. (b) GR distribution of the Elgin swarm sequence. The histogram and dashed line represents the discrete and cumulative magnitude frequency distribution. (c) Goodness of fit (GFT) plot estimating the minimum magnitude of completeness. Circles represent the fit between the observed and synthetic cumulative magnitude-frequency distributions. A 95% GFT threshold was not achieved, therefore 90% and 85% were used for the seismic node detections and the USGS catalog, respectively.

Figure 6: (a) Zoomed-out section of the magnetic lineaments within the EPFS highlighting the general fault trends (red lines) and the placement of swarms within the fault context (Shah et al., 2023). (b) Relocated events identified by the seismic node stations extend beyond a magnetic lineament structure. Cyan circles represent the USGS events while brown circles depict our relocated events. (c) Relocated swarm events are color-coded by depth, with beach balls indicating focal mechanisms and their magnitudes. Preferred nodal planes on focal mechanism solution is highlighted in red. Red arrows depict the maximum principal stress direction (Levandowski et al., 2018), and the white box represents panel in Figure 7a & b.

Figure 7: Cross-sectional view of the swarm events and focal mechanisms (Figure 6c), shown in their original orientation as viewed toward geographic north illustrating a structurally west dipping seismic zone. (a) Depth and Temporal Cross-section along the longitudinal axis (A – A') and (b) latitudinal axis (B – B'). (c) Swarm migration over a short-time period modeled with hydraulic diffusivity (D). White circles represent the 90th percentile distance of the triggered fronts during the first 50 days. (d) Two alternative lines to fit the seismicity front.

Figure S1: (a) The probabilistic power spectral density (PPSD) of background noise recorded at the (a) GT086 and (b) broadband seismometer JKYD. The low and high noise models from (Peterson et al., 1993) are shown as gray curves for reference. The PPSD is computed for the horizontal component of the station's recordings.

Figure S2: RMS of differential time residuals for each event (in seconds), along with the associated errors in longitude (σX), latitude (σY), and depth (σZ) coordinates.

Figure S3: The current locations of seismic nodal deployments from March 19, 2024, aimed at enhancing the monitoring of the earthquake swarm sequence. Among these, six sensors (LSMS, EGTH, PAHC, LSFJ, BWPC, and SJAD) have been in operation since October 2023. The red rectangle in the blow-out map depicts the deployment area, and cyan circles represents the USGS recorded swarm events from December 27, 2021 to March 27, 2024.

Manuscript Received Manuscript Received 1512025